Supporting Information

Dipole-polarized Ni-Bi atomic interface synergistically promotes photocatalytic nitrogen reduction reaction

Yongchong Yu[a], Ping Zhang[a,*], Keyi Chai[a] Xinyu Du[a], Yu Zhang[a], Xiaoping Su[a], Lianbiao Zhao[a,*], Cheng Peng[a], Bin Zhang[a], Lijuan Han[b,*], and Hengjiao Gao[c]

[a]Key Laboratory of Environment-Friendly Composite Materials of the State Ethnic Affairs Commission, Gansu Province Engineering Research Center for Biomass Functional Composite Materials, Key Laboratory for the Utilization of Environment-Friendly Composite Materials and Biomass in Universities of Gansu Province, Gansu Province Research Center for Basic Sciences of Surface and Interface Chemistry, College of Chemical Engineering, Northwest Minzu University, Lanzhou 730030, China.

[b]Gansu Natural Energy Institute, Gansu Academy of Science, Lanzhou 730046, China.

[c]National Key Laboratory of Science and Technology on Vacuum Technology and Physics, Lanzhou Institute of Physics, Lanzhou 730000, China.

S1. Experimental Section

S1.1 Chemicals

Bismuth nitrate pentahydrate ($Bi(NO_3)_3 \cdot 5H_2O$), potassium bromide (KBr), nickel chloride hexahydrate ($NiCl_2 \cdot 6H_2O$) ethylene glycol ($C_2H_6O_2$, EG), ethanol (C_2H_6O), potassium iodide (KI), Mercury Iodide (HgI_2) p-dimethylaminobenzaldehyde ($C_9H_{11}NO$) hydrochloric acid (HCl) and hydrazine chloride ($N_2H_4 \cdot 2HCl$)were purchased from Tianjin Zhiyuan Chemical-Fine Chemical Industry Co., Ltd (Lanzhou, China). Potassium sodium tartrate solution ($KNaC_4H_4O_6$) was purchased from Alarrin Biochemical Technology Co., Ltd (Shanghai, China). All materials were of analytical grade purity and used without further purification. Deionized (DI) water used in experiments was obtained from local water sources.

S1.2 Preparation of photocatalysts

The Ni-BiOBr photocatalyst was synthesized via a solvothermal method. Typically, 0.024 g (0.1 mmol) of $NiCl_2 \cdot 6H_2O$ was initially weighed into a 100 mL beaker, followed by the sequential addition of 1.213 g (2.5 mmol) $Bi(NO_3)_3 \cdot 5H_2O$ and 0.298 g (2.5 mmol) KBr. The mixture was dissolved in 50 mL of ethylene glycol under continuous magnetic stirring for 1 h to ensure homogeneous dispersion. The resultant solution was transferred into a 100 mL Teflon-lined stainless steel autoclave and subjected to solvothermal treatment at 160°C for 12 h. The precipitate was collected through centrifugation, then repeated washing cycles with deionized water and absolute ethanol to remove impurities. The purified product was subsequently dried under a vacuum at 80°C for 8 h, yielding the final 4% Ni-BiOBr catalyst, where the percentage denotes the molar ratio of Ni to Bi. A series of X% Ni-BiOBr catalysts (X = 1-5) with the preparation of $NiCl_2·6H_2O$ precursor quantity within the 0.025-0.125 mmol range while maintaining constant Bi/Br stoichiometry. For comparative studies, pristine BiOBr was synthesized under identical conditions without the cobalt precursor.

S1.3 Characterizations

X-ray diffraction (XRD) (Rigaku Smartlab, Japan) with Cu Ka (k = 1.541 A) radiation source in the range of 5–80 was used to analyze the phase structure of the samples. The absorption properties were studied by UV-Vis diffuse reflectance spectra (UV-Vis DRS) (UV-2600, Japan) in the wavelength range from 200 nm to 800 nm. Morphology and elemental composition were characterized using Thermo Fisher Scientific transmission electron microscopy (TEM), scanning electron microscopy (SEM), High-resolution transmission electron microscopy (HRTEM), and Energy-dispersive spectroscopy (EDS) analysis (China). The surface elements were investigated by X-ray photoelectron spectroscopy (XPS, Thermo Fisher Scientific K-Alpha, China). The Brunauer-Emmett-Teller (BET) surface area was analyzed using a TriStar II 3020. Time-resolved photoluminescence (TRPL) measurements were recorded using an FLS1000 spectrometer with an EPL 375 laser. The in situ infrared testing model is the Nicolet IS50, manufactured by Thermo Scientific, and Electron Paramagnetic Resonance (EPR) measurements were performed under light irradiation on a Bruker A300 instrument. Nitrogen temperature programmed desorption (N_2-TPD) was conducted on a Micromeritics AutoChem II 5080 instrument.

S1.4 Electrochemical analysis

Photoelectrochemical characterization was conducted under 300 W Xe lamp (Beijing Perfectlight PCX-50 C) illumination using a CHI 760E workstation configured with a three-electrode system: Ag/AgCl reference electrode, Pt counter electrode, and catalyst-deposited ITO working electrode (1 cm^2 active area). Use 0.1 M Na_2SO_4 as the electrolyte. According to the Nernst equation (Equation 1), convert the measured values to a normal hydrogen electrode (NHE) potential scale:

$$E_{NHE}(V) = E_{Ag/AgCl} + E^{\ominus}_{Ag/AgCl} \qquad \text{Equation 1}$$

Where $E_{NHE}(V)$ is the converted potential scale vs. NHE, $E_{Ag/AgCl}$ is the measured potential, and $E^{\ominus}_{Ag/AgCl} = 0.1976$ at 298.15 K[1]

S1.5 Calculation of the valence band position of the XPS valence band spectrum

The valence band position relative to the standard hydrogen electrode is calculated according to the following formula：

$$E_{vb,NHE} = \varphi + E_{vb,XPS} - 4.44 \qquad \text{Equation 1}$$

$E_{vb,NHE}$ is the valence band potential of the corresponding standard hydrogen electrode， φ is the work function of the instrument (4.40eV), $E_{vb,\ XPS}$ is the VB-XPS method to measure the valence band potential[2].

S1.6 Determination of ammonia

The concentration of NH_3/NH_4^+ was determined using Nessler’s reagent method. In a typical experiment, 4 mL of supernatant was filtered, then 0.08 mL of potassium sodium tartrate solution ($KNaC_4H_4O_6$, 0.5 $g{\cdot}mL^{-1}$) and 0.08 mL of Nessler's reagent were added to the mixture and allowed to react for 20 minutes before detection. The concentration of NH_3 and NH_4^+ was quantified by monitoring the UV-Vis spectra at 420 nm using standard NH_4Cl concentrations ranging from 0 to 1.5 μmol·mL^{-1}. The standard curve could be defined via linear correlation ($y = 1.1348x + 0.0249$, $R^2 = 0.9998$) (Figure S1).

S1.7 Determination of hydrazine

N_2H_4 production was estimated using the Watt and Chrisp method. A 4.0 g $C_9H_{11}NO$ was accurately weighed and dissolved in 20 mL of HCl and 200 mL of 95% C_2H_6O and allowed to stand for 20 min for color development. After 20 min, the UV-vis spectrum of 2 mL of the color reagent of about 2 mL of the sample solution was recorded at 458 nm, and the N_2H_4 concentration was estimated from the standard calibration curve produced using different N_2H_4 concentrations (0, 1, 2, 3 μmol·mL^{-1}). The standard curve could be defined via linear correlation ($y = 0.6985x + 0.043$, $R^2 = 0.9996$) (Figure S2).

S1.8 Determination of hydrogen

For H_2 calibration, certified gas standards (100 μmol·mol^{-1} in Ar carrier gas) were diluted with Ar to concentrations of 20, 40, 60, 80, and 100 μmol·mol^{-1}. Equal portions of the samples were injected into the GC using an airtight syringe following the same procedure. The resulting calibration curve (Figure S3) shows

S1.9 Theoretical calculations details

DFT calculations were performed using the Materials Studio (MS) software with the generalized gradient approximation (GGA) and the Perdew-Burke-Ernzerhof (PBE) functional[3, 4]. A 3 ×3 ×1 BiOBr supercell is adopted for slab modeling, and the (001) plane is denoted as BiOBr (001). The BiOBr (001) and Ni-BiOBr (001) surfaces were chosen to construct the investigated models. Then, a vacuum of 15Å width was added in the direction normal to the surfaces. An oxygen vacancy is created by removing an oxygen atom from the model. The bottom atomic position was fixed in order to facilitate the convergence, while the surface atomic position was fully relaxed. Geometry optimizations, PDOS, and free energy were performed with a convergence threshold of 10^{-6} eV in energy and 0.05 eV/Å for the force, and the cutoff energy for the plane-wave basis sets was set to 500 eV, respectively. The Brillouin zone was sampled with a 2 × 2 × 1 Gamma-center k-point mesh. The bottom atomic position was fixed to facilitate the convergence, while the surface atomic position was fully relaxed. The free energy of each elementary step was calculated with the adsorption energy (Ead) of the intermediate, as described in Equations 2-3. The more negative value of Eads represents the stronger binding strengths towards the adsorbate.

$$\Delta E_{ad} = E_{surface}+E_{adsorbate} - E_{surface} - E_{adsorbat} \tag{2}$$

$$\Delta G = \Delta E + \Delta E_{ZPE} - T\Delta S \tag{3}$$

Here, $\boldsymbol{E_{surface}}$+$\mathbf{E_{adsorbate}}$, $\boldsymbol{E_{surface}}$, and $\boldsymbol{E_{adsorbate}}$ are the DFT calculated total energy of adsorbed systems, the surface without and with the adsorbate, where $\boldsymbol{\Delta E}$ is the total energy, $\boldsymbol{\Delta E_{ZPE}}$ is the zero point energy, and $\boldsymbol{S}$ is the entropy at 298.15 K. Zero point energy corrections and entropic contributions to the free energies (T=298.15 K).

S1.10 Apparent quantum efficiency (AQE) calculation

Photocatalytic experiments to calculate AQE were carried out in a photocatalytic double-layer quartz bottle reactor. The catalyst mass, solution volume, reaction time, and simulated solar irradiation area were 50 mg, 100 mL, 1 h, and 15.0 cm^2, respectively. The monochromatic filters of 365 nm, 420 nm, 475 nm, 520 nm, and 600 nm were used to filter the light. The light intensity was measured on the PL-MW 2000 photoradiometer. The AQE was calculated through the following equation:

$$\mathrm{AQE} = \frac{N_e}{N_p} = \frac{3 \times N_{NH_3}}{N_p} = \frac{\dfrac{3 \times n_{NH_3} \times N_A}{P \times S \times t}}{hc} \times 100\%$$

where, N_e, N_p and N_{NH3}represent the number of reacted electrons, incident photons, and generated NH_3, respectively; N_A was Avogadro's constant; h was Planck's constant; c, P, S, and t were the speed of light, incident light intensity, irradiated area, and reaction time, respectively.

S1.11 In-situ infrared testing

In situ infrared spectroscopy was employed to detect potential intermediates during the pNRR process. Twenty milligrams of photocatalyst were prepared into a 1 × 1 cm^2 pellet. After securing the pellet, 20 μL of H_2O was dispensed onto the material surface. Ar gas was introduced at 20 sccm to purge the material and gas pathway. Once the baseline stabilised, N_2 was introduced at a flow rate of 40 sccm. Data were collected every 3 minutes, with a total gas flow time of 30 minutes. Following the simulated dark reaction phase, establish the baseline. Upon initiating illumination, collect data at 10-minute intervals throughout the 1-hour exposure period to monitor and document dynamic changes during catalysis.

S1.12 $^{15}N_2$ isotopic labeling experiment

In a 150 mL quartz reactor, 50 mg of catalyst and 100 mL of pure water were added. The reactor underwent repeated vacuum cycles and was purged five times with high-purity argon before introducing high-purity $^{15}N_2$. Following 1 hour of xenon lamp irradiation, the filtrate (0.22 μm) was concentrated to 2 mL under vacuum at 60°C. The pH of the resulting solution was adjusted to 2 using sulphuric acid. The concentration of $15NH_4^+$ was determined using a ^1H NMR spectrometer (Bruker Avance NEO 600).

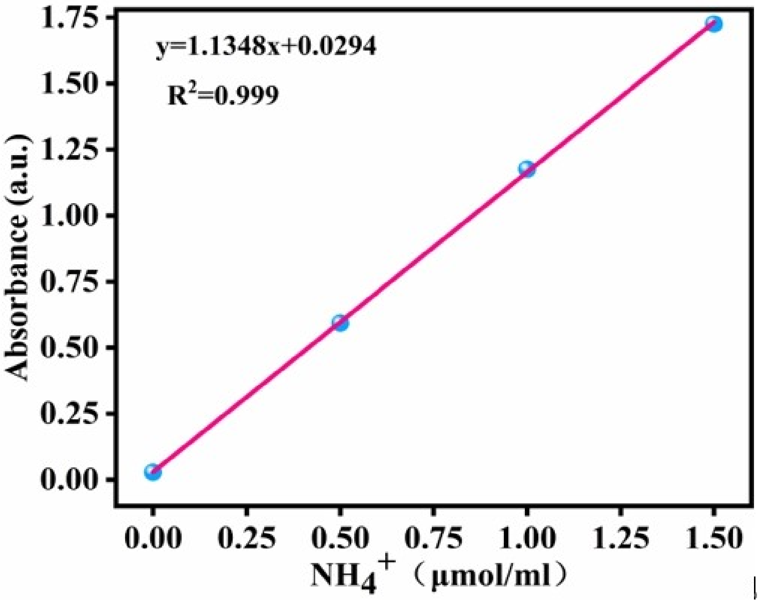

Figure S1. The standard curves were used to calculate the NH_4^+ concentration.

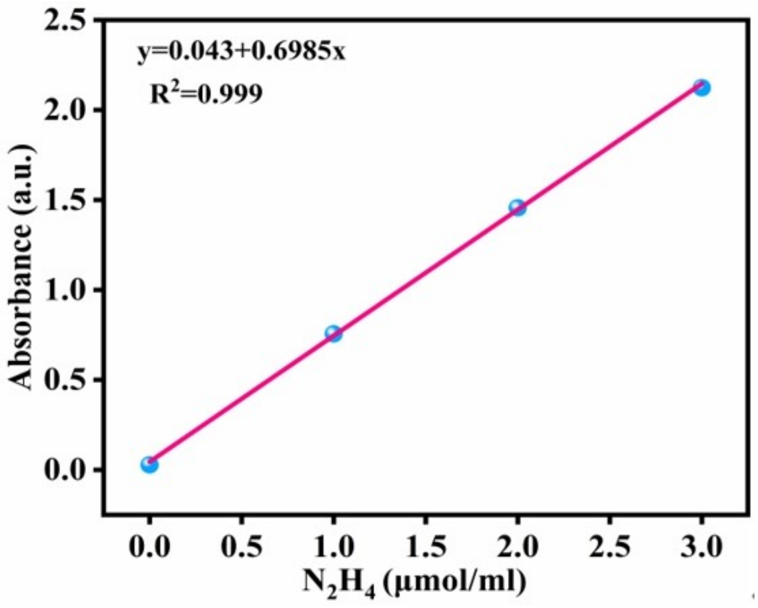

Figure S2. The standard curves were used to calculate the N_2H_4 concentration.

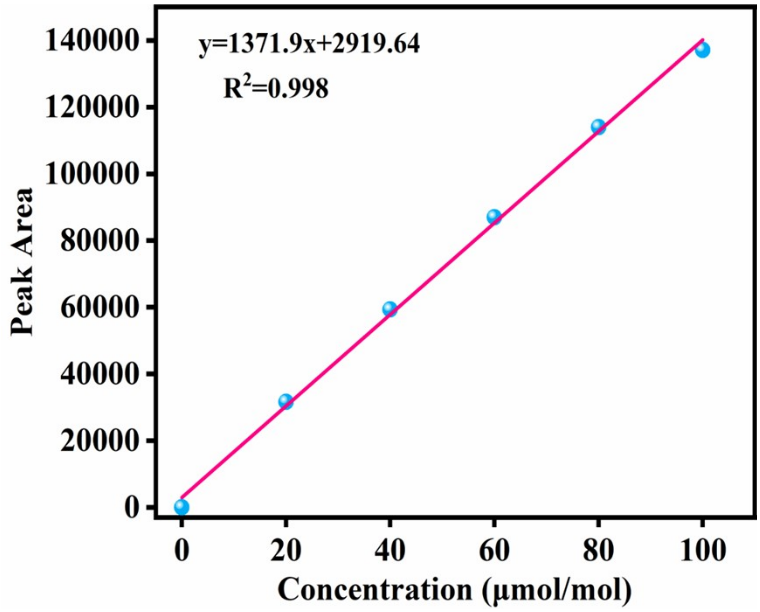

Figure S3. The standard curves were used to calculate the H_2 concentration.

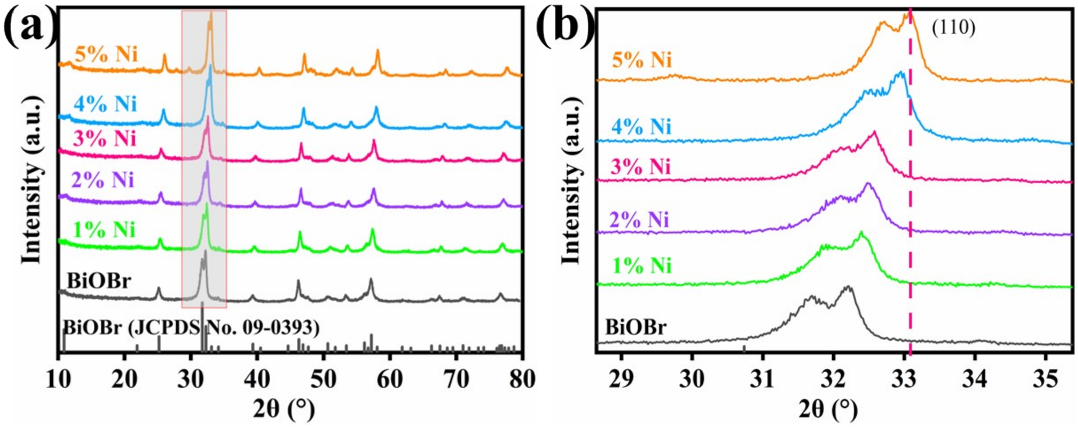

Figure S4. (a) XRD spectra over BiOBr and X%-Ni-BiOBr, (b) Magnified patterns of (110) crystal planes in the 30–34 ° range.

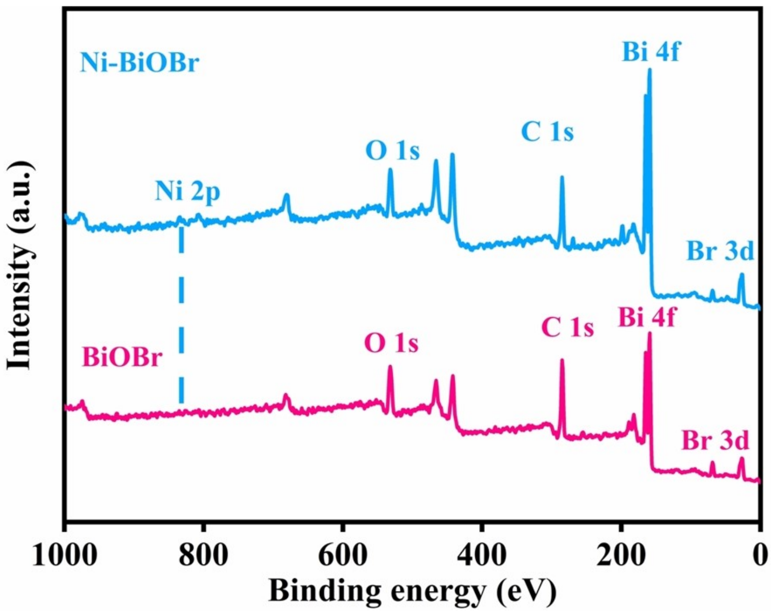

Figure S5. XPS survey spectra for BiOBr and Ni-BiOBr.

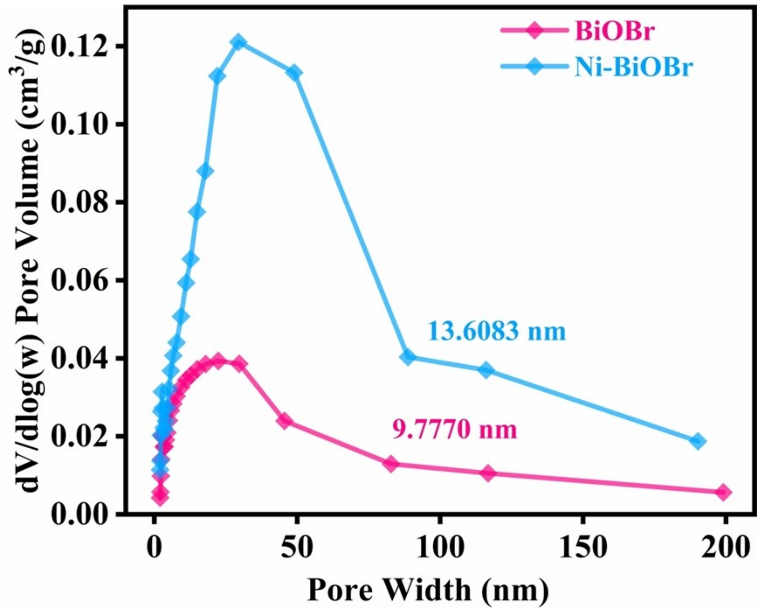

Figure S6. The pore width distribution plots of BiOBr and Ni-BiOBr.

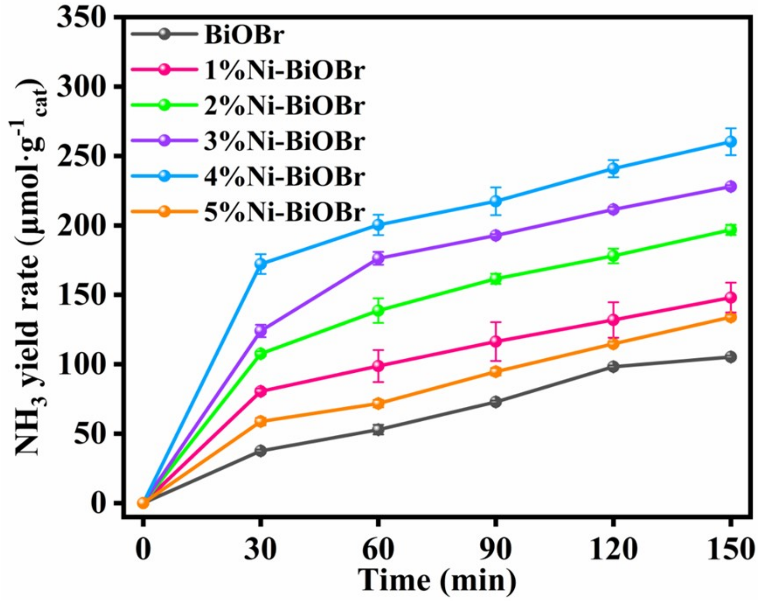

Figure S7 Photocatalytic performance of x%Ni-BiOBr and BiOBr.

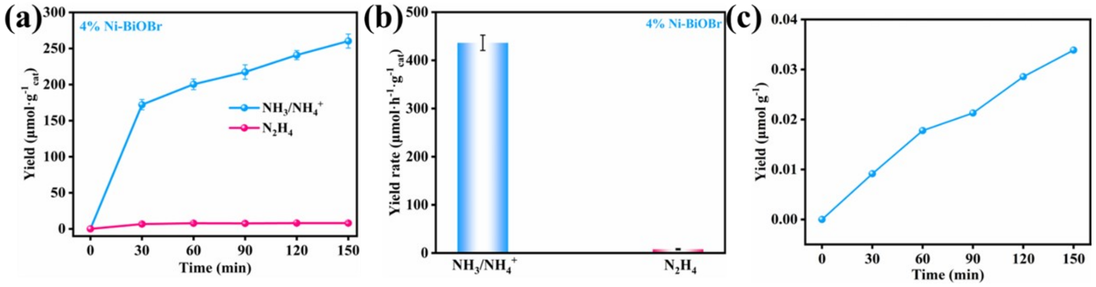

Figure S8. (a) The photocatalytic yield of NH_3/NH_4^+ and N_2H_4 using 4% Ni-BiOBr, (b) Different product rates of 4% Ni-BiOBr, (c) The photocatalytic H_2 yield of 4%Ni-BiOBr.

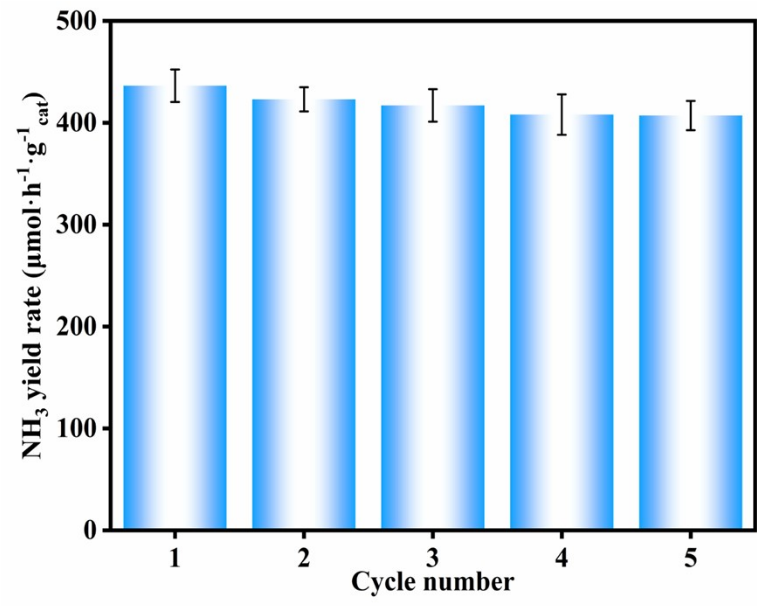

Figure S9. Recycling test number of Ni-BiOBr

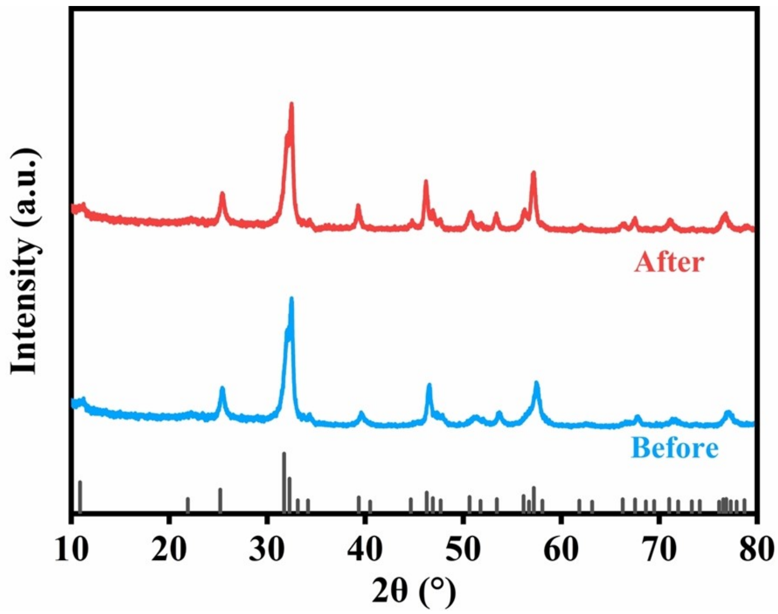

Figure S10. XRD images of Ni-BiOBr before and after cycling experiments.

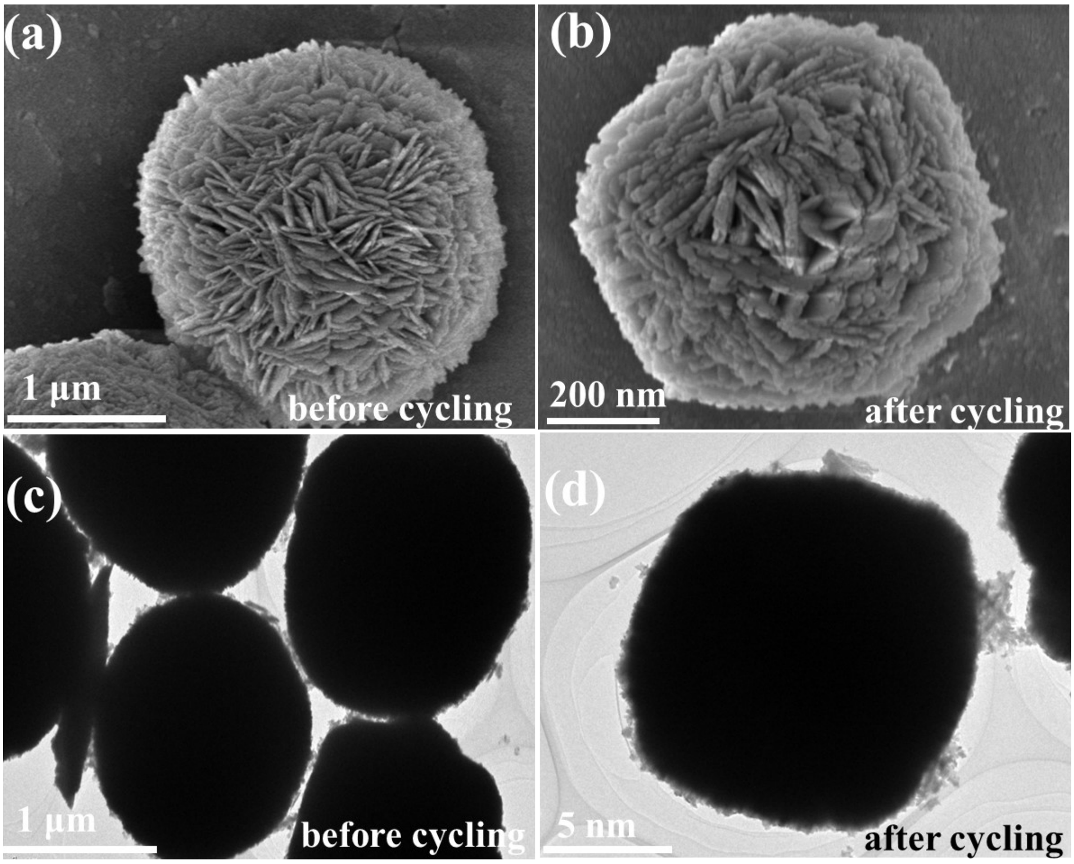

Figure S11. (a, b) SEM and (c, d) TEM images of Ni-BiOBr before and after recycling experiments.

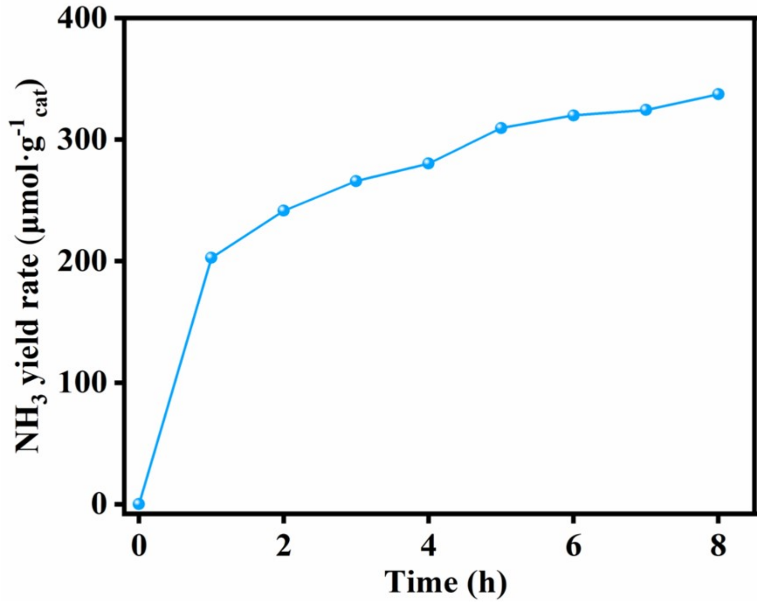

Figure S12. Photocatalytic NH$_3$ yields by Ni-BiOBr in 8 h.

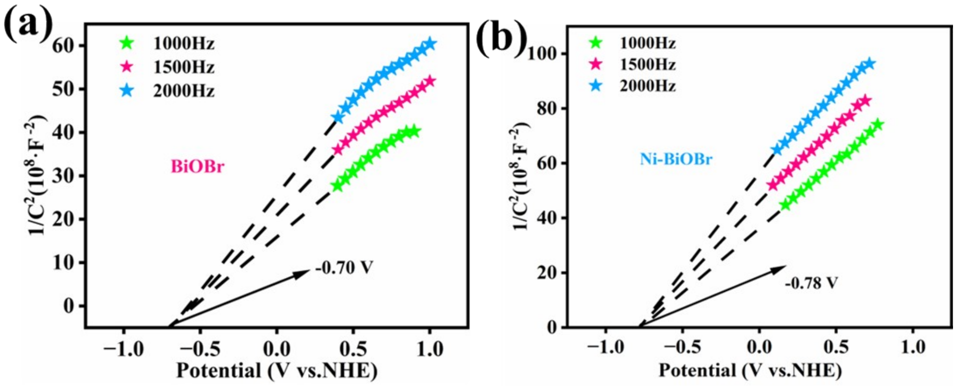

Figure S13. Mott-Schottky profiles of (a) BiOBr and (b) Ni-BiOBr.

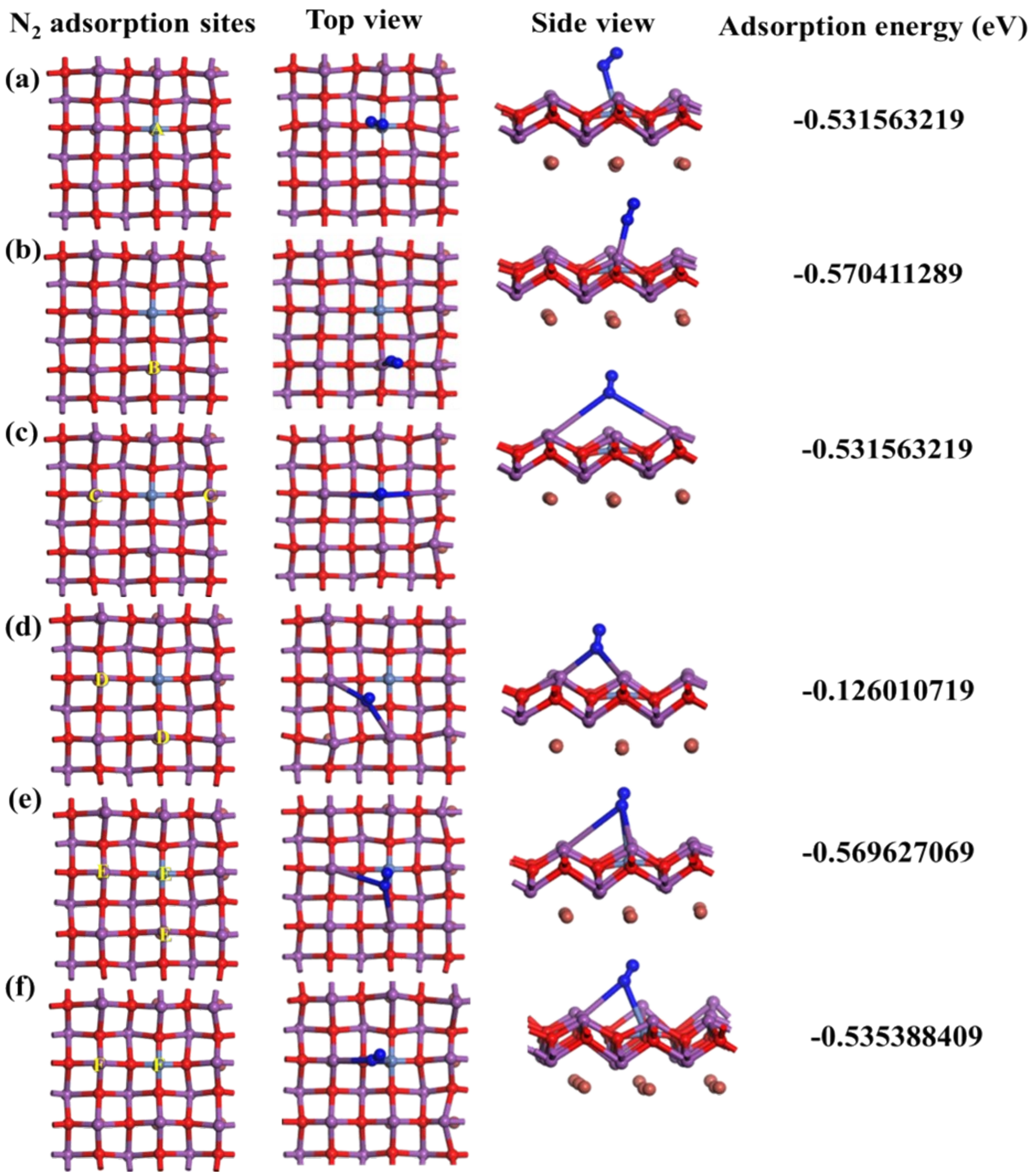

Figure S14. The adsorption positions and corresponding adsorption energies of five types of N_2 on the Ni-BiOBr model. The red, purple, brown, light blue, and dark blue spheres represent O, Bi, Br, Ni, and N atoms, respectively.

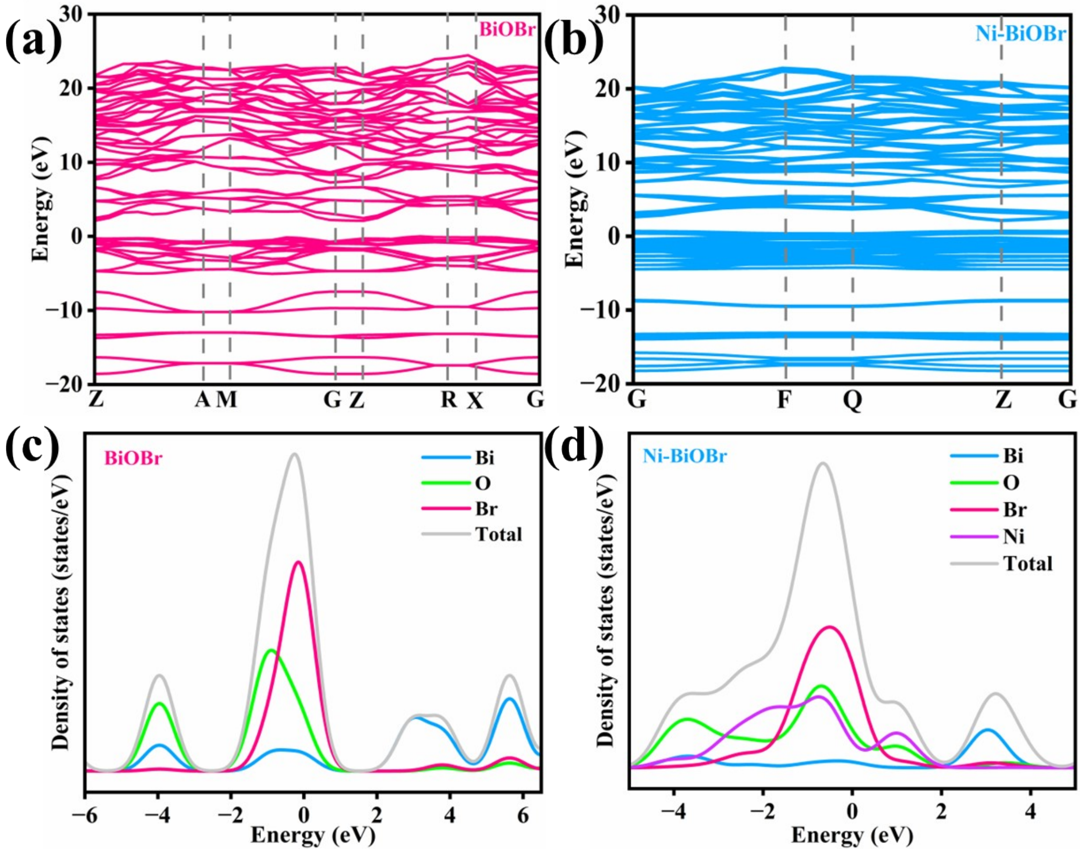

Figure S15. Band structure of (a) BiOBr and (b) Ni-BiOBr, Calculated density of states of (c) BiOBr and (d) Ni-BiOBr.

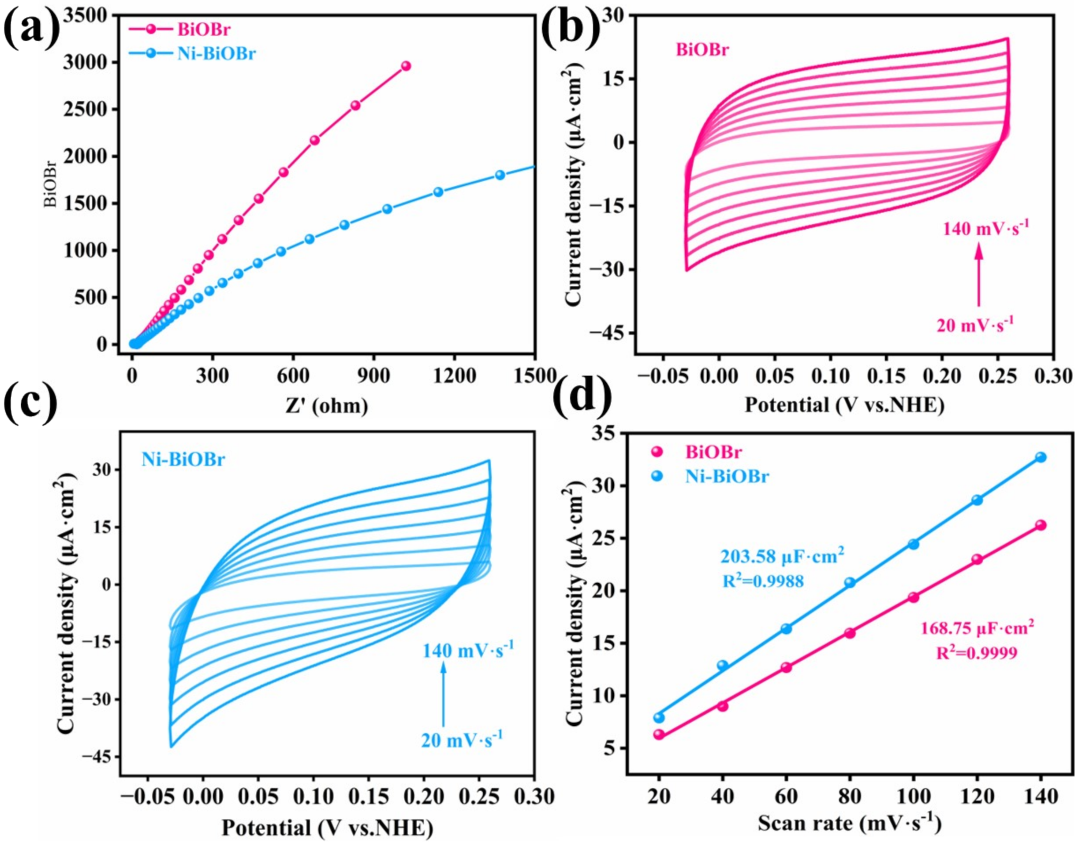

Figure S16. (a) EIS spectra of BiOBr and Ni-BiOBr, CV curves of (b) BiOBr and (b) Ni-BiOBr at different scan rates, (d) The fitting curve between the current density and scan rate.

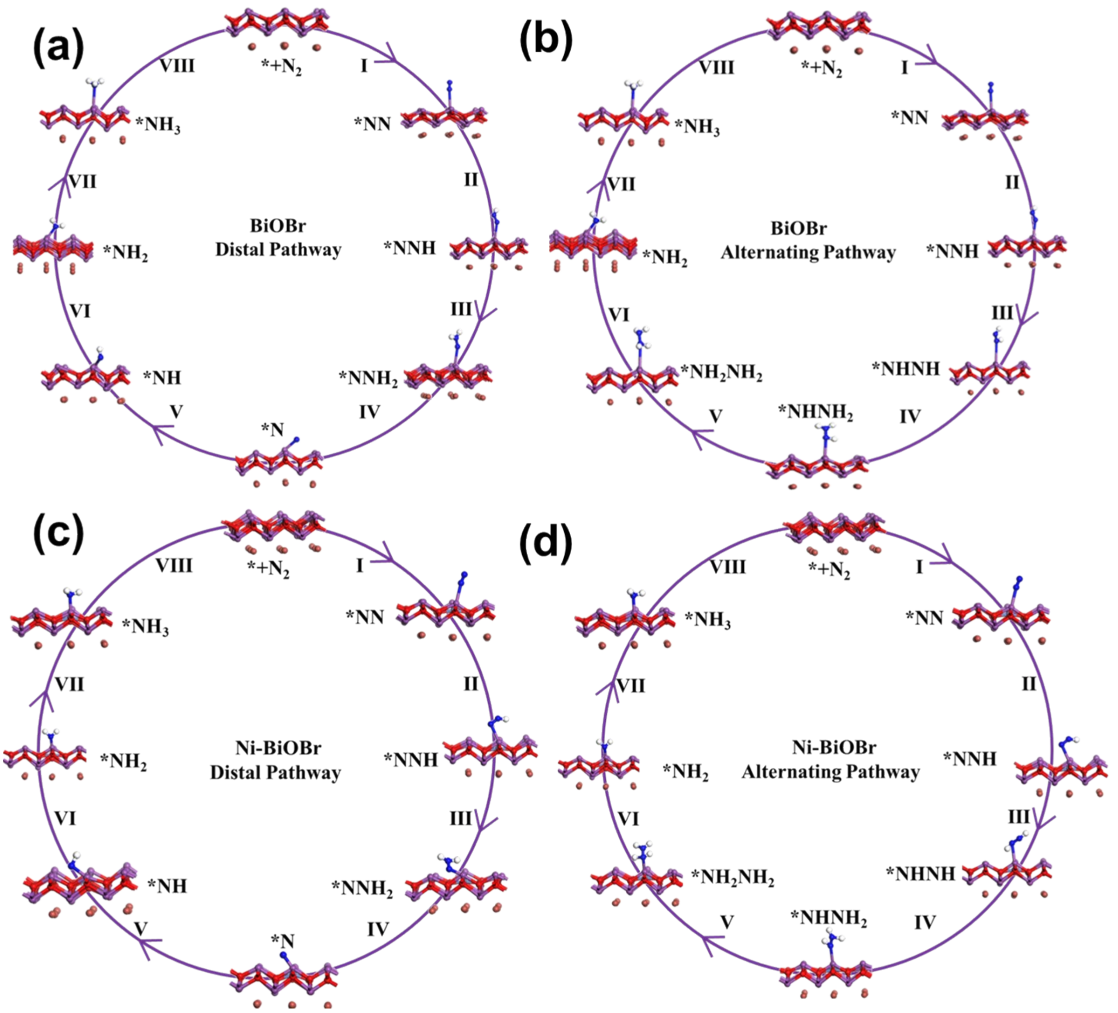

Figure S17. The pathway of (a) distal pathway BiOBr, (b) alternating pathway of BiOBr, (c) distal pathway Ni-BiOBr, and (d) alternating pathway of Ni-BiOBr. The red, purple, brown, light blue, and dark blue spheres represent O, Bi, Br, Ni, and N atoms, respectively.

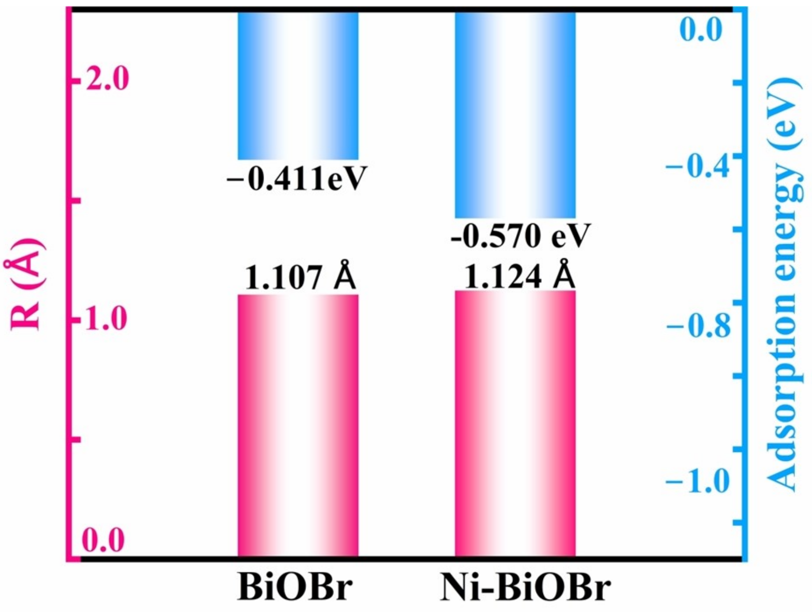

Figure S18. Calculate the adsorption energy and N ≡ N length of N_2 on BiOBr and Ni-BiOBr.

Table S1. ICP-AES results of 4%Ni-BiOBr

Samples	**Theoretical Ni/Bi (Atomic molar ratio, %)**	**Theoretical Ni element content (Wt.%)**	**Real element content of Ni (Wt.%)**
4% Ni-BiOBr	4.0	0.7980	0.4980

Table S2. Calculate the BET surface area and Pore volume of BiOBr and Ni-BiOBr.

Sample	**surface area(m^2/g)**	**Pore volume (cm^3/g)**
BiOBr	16.9803	0.043443
Ni-BiOBr	32.9582	0.112464

Table S3 Comparison of the performance of BiOBr-based photocatalysts related to photocatalytic nitrogen reduction

Photocatalysts	**sacrificial reagent**	**NH_3 yield**	**Ref.**
Ni-BiOBr	**-**	**436.38 μmol $h^{-1}\cdot g^{-1}$**	**This work**
Bi-BiOBr/Cl	10% methanol	2.07 mmol $h^{-1}\cdot g^{-1}$	5
BiOBr/g-C_3N_4	-	164.7 μmol $h^{-1}\cdot g^{-}$	6
Ru-BiOBr-NF	-	121.9 μmol $h^{-1}\cdot g^{-1}$	7
MoO_2/BiOBr	-	176.66 μmol $h^{-1}\cdot g^{-1}$	8
N-GY-Bi/BiOBr	-	5.68 μmol $h^{-1}\cdot g^{-1}$	9
BiOBr/$Bi_4O_5Br_2$		66.87 μmol $h^{-1}\cdot g^{-1}$	10
Pt/BOB-VO	-	23.8 μmol $h^{-1}\cdot g^{-1}$	11
CL@BiOBr-OV/Au	-	2.64 mmol $h^{-1}\cdot g^{-1}$	12
BiOBr-Fe-S-1	-	46.1 μmol $h^{-1}\cdot g^{-1}$	13
Pd-EG-BiOBr	-	124.63 μmol $h^{-1}\cdot g^{-1}$	14
Bi/BiOBr	0.025 M Na_2SO_3 (aq)	55.65 μmol $h^{-1}\cdot g^{-1}$	15
Vo-BiOBr	-	54.7 μmol $h^{-1}\cdot g^{-1}$	16

Table S4. The fitted equation for the decay lifetime curves of the samples

Sample	**B_1 (%)**	**τ_1 (ns)**	**B_2 (%)**	**τ_2 (ns)**	**τ_{Ave} (ns)**
BiOBr	51.23	1.0604	48.77	8.6312	4.7527
Ni-BiOBr	53.50	0.9055	46.50	7.8253	4.1235

References

1. X. Song, W. Li, X. Liu, Y. Wu, D. He, Z. Ke, L. Cheng, C. Jiang, G. Wang, X. Xiao and Y. Li, *Journal of Energy Chemistry*, 2021, **55**, 154-161.
2. X. Gao, K. Xu, H. He, S. Liu and X. Zhao, *Journal of Industrial and Engineering Chemistry*, 2022, **111**, 129-136.
3. J. P. Perdew, J. A. Chevary, S. H. Vosko, K. A. Jackson, M. R. Pederson, D. J. Singh and C. Fiolhais, *Physical Review B*, 1992, **46**, 6671-6687.
4. S. Froyen, *Physical Review B*, 1989, **39**, 3168-3172.
5. S. Lv, F. Guo, K. Li, D. Wang, H. Gao and C. Song, *Journal of Colloid and Interface Science*, 2025, **677**, 831-841.
6. L. Zhang, M. Jiang, H. Tian, S. Liu, X. Zhou, H. Liu, S. Gan, S. Che, Z. Chen, Y. Li, T. Wang, G. Wang and C. Wang, *ACS Sustainable Chemistry & Engineering*, 2024, **12**, 2028-2040.
7. Y. Xia, X. Xia, L. Chen, R. Liang, G. Yan and S. Liang, *Applied Catalysis B: Environment and Energy*, 2024, **349**, 123859.
8. Z. Chen, Z. Huang, J. Yang, Y. Meng, B. Xie, Z. Ni and S. Xia, *Journal of Materials Chemistry A*, 2024, **12**, 16877-16891.
9. X. Huang, M. Sun, M. Humayun, S. Li, J. Zhao, H. Chen and Z. Li, *Journal of Alloys and Compounds*, 2024, **976**, 173025.
10. H. Wang, Z. Chen, Y. Shang, C. Lv, X. Zhang, F. Li, Q. Huang, X. Liu, W. Liu, L. Zhao, L. Ye, H. Xie and X. Jin, *ACS Catalysis*, 2024, **14**, 5779-5787.
11. G. Ren, M. Shi, Z. Li, Z. Zhang and X. Meng, *Applied Catalysis B: Environmental*, 2023, **327**, 122462.
12. X. Wang, B. Wang, S. Yin, M. Xu, L. Yang and H. Sun, *Journal of Cleaner Production*, 2022, **360**, 132162.
13. X. Chen, X. Zhang, Y.-H. Li, M.-Y. Qi, J.-Y. Li, Z.-R. Tang, Z. Zhou and Y.-J. Xu, *Applied Catalysis B: Environmental*, 2021, **281**, 119516.
14. J. Liu, F. Li, J. Lu, R. Li, Y. Wang, Y. Wang, X. Zhang, C. Fan and R. Zhang, *Journal of Colloid and Interface Science*, 2021, **603**, 17-24.

15. Y. Huang, Y. Zhu, S. Chen, X. Xie, Z. Wu and N. Zhang, *Advanced Science*, 2021, **8**, 2003626.
16. X. Xue, R. Chen, H. Chen, Y. Hu, Q. Ding, Z. Liu, L. Ma, G. Zhu, W. Zhang, Q. Yu, J. Liu, J. Ma and Z. Jin, *Nano Letters*, 2018, **18**, 7372-7377.